AIAA JOURNAL
Vol. 35, No. 1, January 1997

Velocity Measurements over a Pitching Airfoil

H. Oshima* and B. R. Ramaprian†
Washington State University, Pullman, Washington 99164-2920

The results of instantaneous velocity measurements on the suction side of a two-dimensional NACA 0015 airfoil pitching at constant angular velocity about its quarter-chord spanwise axis are presented. The experiments were performed in an open-surface water channel at two Reynolds numbers (5.4×10^4 and 1.5×10^5) using the technique of particle image velocimetry for the measurement of the instantaneous velocity field. The velocity (and hence vorticity) data obtained in these experiments supplement the surface pressure data obtained in earlier experiments on the same model under the same conditions. The data have been used to obtain quantitative information on the evolution of the flow structure over the pitching airfoil. They have also been compared with results obtained earlier at a low Reynolds number (1.8×10^4) to examine in some detail the Reynolds number effect on the flow structure. The study has shown that the dynamic-stall vortex (DSV) still consists of the rolled-up shear layer along with remnants of several vortices generated by the shear layer instability, as observed at low Reynolds numbers, and that the increase of lift at post-static stall incidences is still due to the presence of vortical structures close to the surface, till they are eventually ejected prior to the occurrence of dynamic stall. Also, the dominant topological features of the flow in the leading-edge region prior to dynamic stall closely resemble the numerical predictions recently reported in the literature for low Reynolds number flows. However, the DSV at high Reynolds numbers is more compact, has fewer remnants of vortical structures, and is ejected abruptly from the airfoil surface in a direction almost normal to the surface. The detailed quantitative experimental data have been archived and are available to any interested user.

Nomenclature

C_l = coefficient of lift, $l/[(\rho U_\infty^2/2)c]$
C_p = coefficient of surface pressure, $(p - p_\infty)/(\rho U_\infty^2/2)$
c = airfoil chord
l = lift force per unit span
n = coordinate direction normal to the airfoil surface
p = pressure at any point on the model surface
p_∞ = freestream static pressure
Re = Reynolds number, $U_\infty c/\nu$
$S_{n,s}$ = velocity gradient, $\partial V_n/\partial s$
$S_{s,n}$ = velocity gradient, $\partial V_s/\partial n$
s = coordinate direction along the airfoil surface, measured from the nose
s_c = s coordinate of the center of the dynamic stall vortex
t = time
U_∞ = freestream velocity
V_n = velocity component along the n direction
V_s = velocity component along the s direction
x = chordwise direction
α = angle of incidence
α^+ = nondimensional pitch rate, $\omega c/U_\infty$
$\epsilon_{s,n}$ = shear strain rate in the s–n plane, $(\partial V_s/\partial n + \partial V_n/\partial s)$
ν = kinematic viscosity
ρ = density
Φ = stream function
ω = angular velocity of pitching
ω_z = spanwise vorticity, $(\partial V_n/\partial s - \partial V_s/\partial n)$

Introduction

THE unsteady flow over a two-dimensional airfoil pitching at a constant angular velocity about a spanwise axis has been studied by a number of investigators in recent years. The interest in this flow configuration has primarily been driven by the desire to understand unsteady vortex dynamics and the phenomenon of dynamic stall. However, practically all experimental studies of these flows have so far been limited to qualitative flow visualization, measurement of surface pressure distribution, or a limited amount of near-surface velocity measurements over the wing. A few exceptions to these are the unsteady velocity field measurements at low Reynolds numbers around a NACA 0012 airfoil by Shih et al.[1] and our own recent experiments[2] on a NACA 0015 airfoil. On the other hand, recent computational studies such as those of Ghia et al.,[3] Visbal and Shang,[4] and Choudhuri et al.[5] have resulted in a detailed description of the surface pressure as well as the flowfield around the airfoil. However, a complete set of experimental data is not available for the verification or further development of such numerical models.

The present work formed a part of an extensive research program on the study of the unsteady aerodynamics and dynamic stall of a pitching airfoil of NACA 0015 profile. The studies under this program were performed in an open-surface water channel specially designed and constructed for this purpose. The experiments were conducted at several Reynolds numbers in the range from 1.8×10^4 to 2.3×10^5. In all of the experiments, the airfoil was pitched about its spanwise $c/4$ axis at constant angular velocity. The nondimensional pitching rate α^+ varied from 0.036 to 0.2 in these experiments. The velocity measurements at the lowest Reynolds number of 1.8×10^4, which were made using the technique of particle image velocimetry (PIV) in the very early phase of the research program, have been reported separately.[2] The surface pressure data for several Reynolds numbers and pitch rates in the preceding range have also been reported in an earlier publication.[6] The present paper describes PIV measurements of the evolution of the instantaneous velocity field at two of the highest Reynolds numbers (5.4×10^4 and 1.5×10^5) in the preceding range. These correspond to nominal test section velocities of 10 and 30 cm/s, respectively. The value of α^+ was 0.072 in both experiments. Surface pressure data corresponding to these flow conditions are available from Ref. 6. It has therefore become possible to study the flow evolution in these two cases by using the PIV data in conjunction with the corresponding surface pressure data. This is a distinguishing feature of the present work.

The earlier pressure measurements in the present water channel at Reynolds numbers larger than 3×10^5 revealed interestingly that the boundary layer over the airfoil model undergoes very early transition from laminar to turbulent flow near the leading edge, presumably

Received Dec. 27, 1995; revision received Aug. 17, 1996; accepted for publication Aug. 19, 1996; also published in *AIAA Journal on Disc,* Volume 2, Number 1.

*Graduate Student, School of Mechanical and Materials Engineering; currently Design Engineer, M.S. FM5-43, Intel Corporation, 1900 Prairie City Road, Folsom, CA 95630.

†Professor, School of Mechanical and Materials Engineering, P.O. Box 642920. Member AIAA.

due to the combination of the relatively high level of freestream turbulence in the water channel (about 1.5–2%) and externally imposed unsteadiness.[6] The early transition resulted in almost complete elimination of the so-called leading-edge separation bubble. In fact, the pressure distribution and lift data obtained under these conditions in Ref. 6 closely resembled those obtained by other investigators in experiments at much higher Reynolds numbers ($\approx 2 \times 10^6$). The detailed information on the instantaneous velocity and vorticity distributions obtained in this study at the two Reynolds numbers above 3×10^5, together with such data obtained in Ref. 2 at a Reynolds number of 1.8×10^4, would therefore be particularly useful for studying transition effects on the unsteady flow. A further important feature of the present work is that PIV data have been obtained with spatial and temporal resolution higher than has been achieved in the past. This became possible because of the use of a large model of 35 cm (1 ft) chord in a relatively large test section, namely, 1×0.7 m (3×2 ft) and the use of water as the working fluid.

Experimental Details

Experimental Facility

The experiments were performed in a free-surface water channel with a test section 4 m (12 ft) long and 1×0.7 m (3×2 ft) in cross section. The test section velocity in this facility can be varied from 0–0.5 m/s (0–1.5 ft/s). The freestream turbulence level is about 1.2% at a test section velocity of 30 cm/s (1 ft/s) and 2.5% at a velocity of 5 cm/s (0.17 ft/s). For a complete description of the facility, see Conger and Ramaprian.[7] The entire channel is seeded with micron-sized particles of controlled size to allow PIV measurements.

The airfoil studied is a NACA 0015 profile of 35 cm (14 in.) chord and 67 cm (27 in.) span. This is the same model on which pressure measurements were made in the earlier study reported in Ref. 6. It is formed from extruded aluminum stock and painted dull black to prevent glare and reflection during flow visualization. Figure 1 shows a schematic of the airfoil mounting and pitching arrangement. The airfoil is mounted with its span vertical in the test section. It is provided with a circular transparent end plate that just dips into the water. The end plate prevents wave effects at the free surface and also provides an unobstructed and distortion-free view of the flowfield around the airfoil. The end plate is mounted in a circular bearing of 65-cm (26-in.) diam carried by a rectangular aluminum plate. The bearing allows the end plate to be rotated about its vertical axis clockwise or counterclockwise at any desired angular velocity over an angle of 90 deg, via a chain drive, by a computer-controlled stepper motor. The chain drive arrangement leaves the top of the end plate optically clear, for flow visualization from the top. An encoder mounted on the shaft of the stepper motor measures the angle of incidence of the airfoil. The airfoil is mounted with its quarter-chord ($c/4$) axis passing through the center of the end plate. Hence the rotation of the end plate about its center causes the airfoil to pitch about its $c/4$ axis. More details of the model assembly are provided in Ref. 7.

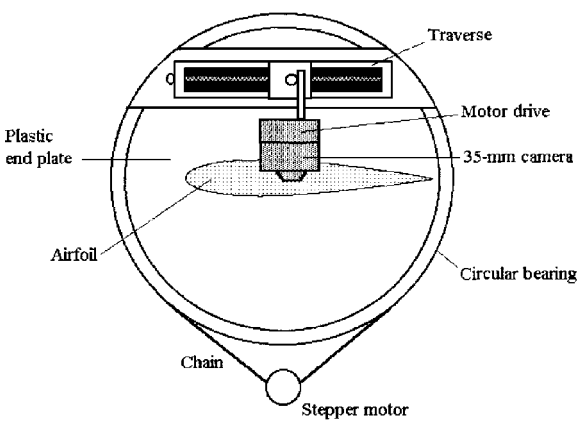

Fig. 1 Schematic of the airfoil mounting and pitching arrangement.

Instrumentation

Because phenomena of interest to this study occur primarily on the suction side of the airfoil, PIV measurements were obtained only on this side of the airfoil. However, surface pressure data are available for both sides of the airfoil. The PIV data were obtained at the midspan plane of the airfoil. This was achieved by illuminating this plane by a laser light sheet. Figure 2 shows a schematic of the optical setup used. In the lower Reynolds number experiment, fluorescent polystyrene particles of 2-μ (0.8×10^{-4} in.) diam were used for seeding the flow and a 4-W argon ion laser was used as the light source. Since a shorter exposure time was required in the higher Reynolds number experiment, this source was replaced by a more powerful 20-W copper-vapor laser in that experiment. Also, the seed particles were replaced by 30-μ (1.2×10^{-3} in.) nonfluorescent particles (supplied by Optimage Ltd. of Edinburgh, Scotland, United Kingdom). These particles were found to be less expensive and superior in performance. In both the experiments, a rotating shutter was used in the path of the laser beam to obtain laser pulses at the desired frequency. A Nikon F-3 35-mm camera equipped with a motor drive was used for taking the multiple-exposure particle image photographs. The motor drive allowed photographs to be obtained at a rate of up to four frames per second. Kodak Tri-X ASA 400 black and white film was used for the photography. The camera was mounted on top of the circular end plate, aiming directly downward (see Fig. 1) and was moved with the airfoil. The velocity data were thus obtained in a coordinate frame moving with the airfoil. The movement of the airfoil was synchronized with the camera control, and in both the experiments, a total of 36 photographs were obtained at equal intervals over the pitching range of 0 to about 29 deg. The angular resolution was thus approximately 0.8 deg. The rotating shutter was set to provide four exposures during each opening of the camera shutter. For details on camera and shutter settings and the experimental procedure, reference may be made to Oshima.[8]

As in the first PIV experiments reported in Oshima and Ramaprian,[2] to achieve good spatial resolution and reach points closer to the airfoil surface, the flowfield on the suction side of the airfoil was subdivided into three regions, namely, front, mid, and aft

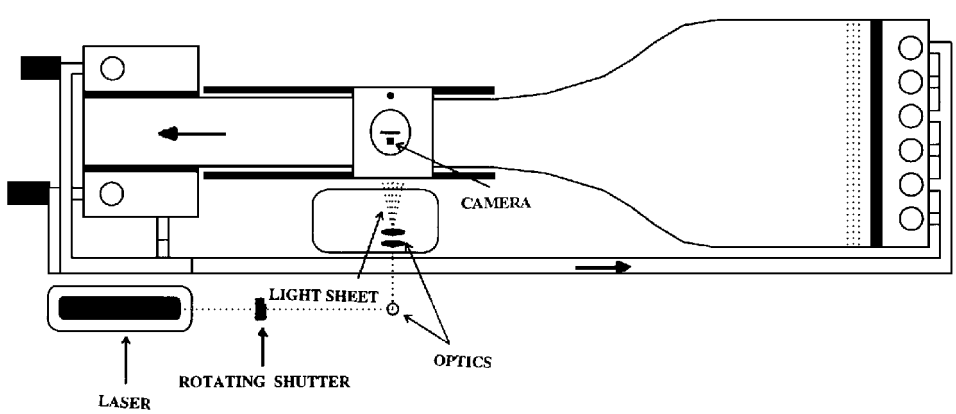

Fig. 2 Schematic of the optical setup.

Table 1 Spatial and temporal resolution of the PIV system

Reynolds number	Spatial averaging (inner region)	Spatial averaging (outer region)	Temporal averaging (front region)	Temporal averaging (mid and aft regions)
5.4×10^4	$0.009c \times 0.007c$	$0.018c \times 0.014c$	1/22.5 s (0.053 deg)	1/15 s (0.080 deg)
1.5×10^4	$0.009c \times 0.007c$	$0.018c \times 0.014c$	1/64 s (0.056 deg)	1/40 s (0.090 deg)

regions, and each region was zoomed in and photographed during three separate pitching realizations. The velocity fields computed for the three regions from the three different realizations were later combined and treated as part of a single realization. Although this procedure sometimes introduced some discontinuities in the measured velocity field between two adjacent regions, it was a tradeoff needed to achieve higher spatial resolution. The problem of mismatch on the whole was, however, not severe because the larger structures in the flow were found to be fairly repetitive from one realization to another, at least prior to the occurrence of dynamic stall.

The primary purpose of these experiments was to obtain the detailed evolution of the instantaneous flowfield during a typical realization. The preceding procedure was found to be satisfactory in achieving this. No attempt was made to average the results over a number of realizations because this would have masked the behavior of the smaller-scale activities, such as shear layer instability, etc., which do not repeat in a deterministic manner during different realizations. Note that the present velocity data and the earlier (phase-averaged) pressure data can be used together and for comparison with computational fluid dynamics results, as long as the interest is in the larger-scale motions.

The multiple-exposed photographs were scanned and processed using the PIV interrogation system developed in house at Washington State University. This system uses the well-known autocorrelation method to obtain the velocity vectors. Velocity vectors were computed twice, once using a fine grid to obtain a total of 1600 velocity vectors from each photograph, and a second time using a coarse grid to obtain 400 velocity vectors. The fine grid results were used for the region adjacent to the wall where the velocities are smaller. The coarse grid data were used for the outer region with larger velocities. An interactive postprocessing program was used to select and match these results from the two grids and to detect and correct/replace any bad velocity vectors. Also, the PIV system used was not inherently capable of detecting flow reversals. This issue was resolved during postprocessing by the operator, with the assistance of a video record of the flow that had been obtained simultaneously with the photographic record. Other postprocessing programs were used to compute the velocity components V_s and V_n, spanwise vorticity ω_z, stream function Φ, the shear strain rate $\epsilon_{s,n}$, and other quantities of interest, from differentiating/integrating the measured velocity field. In all of these calculations, the coordinate system has been assumed to be nearly Cartesian. This assumption is adequate for the purpose of the discussion presented in this paper. The reader can, of course, use the archived raw data and the geometry of the airfoil to recalculate all of the kinematic quantities, without making the preceding assumption. The PIV system and the details of the entire procedure used in the present study are described briefly in Ref. 2 and in more detail in Ref. 8.

Errors and Uncertainties

Issues concerning two-dimensionality of the flow and errors due to blockage in the present facility have been discussed in detail in Ref. 6 and will not be repeated here. It will only be mentioned here that the flow in the midregion of the airfoil has been shown to be acceptably two-dimensional (a spanwise variation in peak suction pressure of less than 4.3%) and that typical blockage effects on lift are less than 15% at the maximum incidence of interest to this paper. As pointed out in Ref. 6, these conditions represent a compromise between large model size (hence large Reynolds number and the best possible spatial and temporal resolution of measurements) and good flow quality.

The details of spatial and temporal averaging used in the processing of the PIV images for the two experiments are summarized in Table 1.

Note further that particle photographs were obtained at time intervals of 0.7 s at the lower Reynolds number and 0.25 s at the higher Reynolds number. These correspond to 0.84 and 0.9 deg, respectively, in incidence interval. The overall uncertainty in the velocity measurements is about 2% of the maximum velocity in the flow. Based on the observed scatter in the velocity data, it is reasonable to assume an uncertainty of 10% in the vorticity calculations. It is also important to state that velocity data could not be obtained closer than 2.4 mm (0.1 in.) from the wall, though they can be estimated approximately from extrapolation to the wall. The uncertainties in velocity and vorticity estimates are higher in this region. The uncertainty in the estimation of the stream function is not more than 10%.

PIV Results

Many similarities were found in the basic as well as the gross features of the flow at the two Reynolds numbers studied. For this reason and also in the interest of brevity, results will be presented mostly for the higher Reynolds number experiment. However, a few typical results will be shown for the lower Reynolds number flow also. It is also important to note that although the velocities were measured in a noninertial coordinate system (spinning at a constant angular velocity about the pitching axis of the airfoil), the effect of rotation of the coordinate axes has negligible effect on the results at the very low pitching rate of $\alpha^+ = 0.072$ studied.

Evolution of the Velocity and Vorticity Fields

Figure 3 displays a few typical instantaneous velocity and vorticity fields on the suction side over the entire airfoil, obtained at the Reynolds number of 1.5×10^5. The examples cover the interval from $\alpha = 20.9$ to 27.8 deg. Figures 4a and 4b show the corresponding pressure and lift data, taken from Conger and Ramaprian.[6] At incidences below 21 deg, the flow features evolve slowly and are qualitatively similar to those at 20.9 deg. Thus, at these lower incidences, the contours of very high negative vorticity are very narrow and stretched out and are nearly parallel to the airfoil surface, especially over the front half of the airfoil. The peak vorticity decreases in magnitude and the vorticity contours spread outward a little more toward the trailing edge, but the vortical region is still essentially adjacent to the airfoil surface. This results in continued lift generation with incidence. In fact, pressure distributions and lift, shown in Figs. 4a and 4b, behave essentially as in steady flow, except that the peak suction pressure and lift continue increasing with incidence. In other words, they can be considered to exhibit almost an extension of the steady-flow behavior.

The thickening of the vortical region in the mid-to-aft region of the airfoil is due to the presence of a small layer of reverse flow near the airfoil surface. This can be seen from the velocity field at $\alpha = 20.9$ deg. In fact, this region of reverse flow was first observed in the trailing-edge region at an incidence of about 18 deg. It was found to spread subsequently in the upstream direction thickening the shear layer in the mid-to-aft regions, as the incidence increased from 18 to 20.9 deg.

Beyond $\alpha = 20.9$ deg, vorticity contours at around $x/c = 0.1$ start to bulge out, producing a locally closed set of negative (clockwise) vorticity contours, which is indicative of the inception of the so-called leading-edge vortex (LEV), which is also often referred to as the primary vortex. The LEV then continues to grow in size

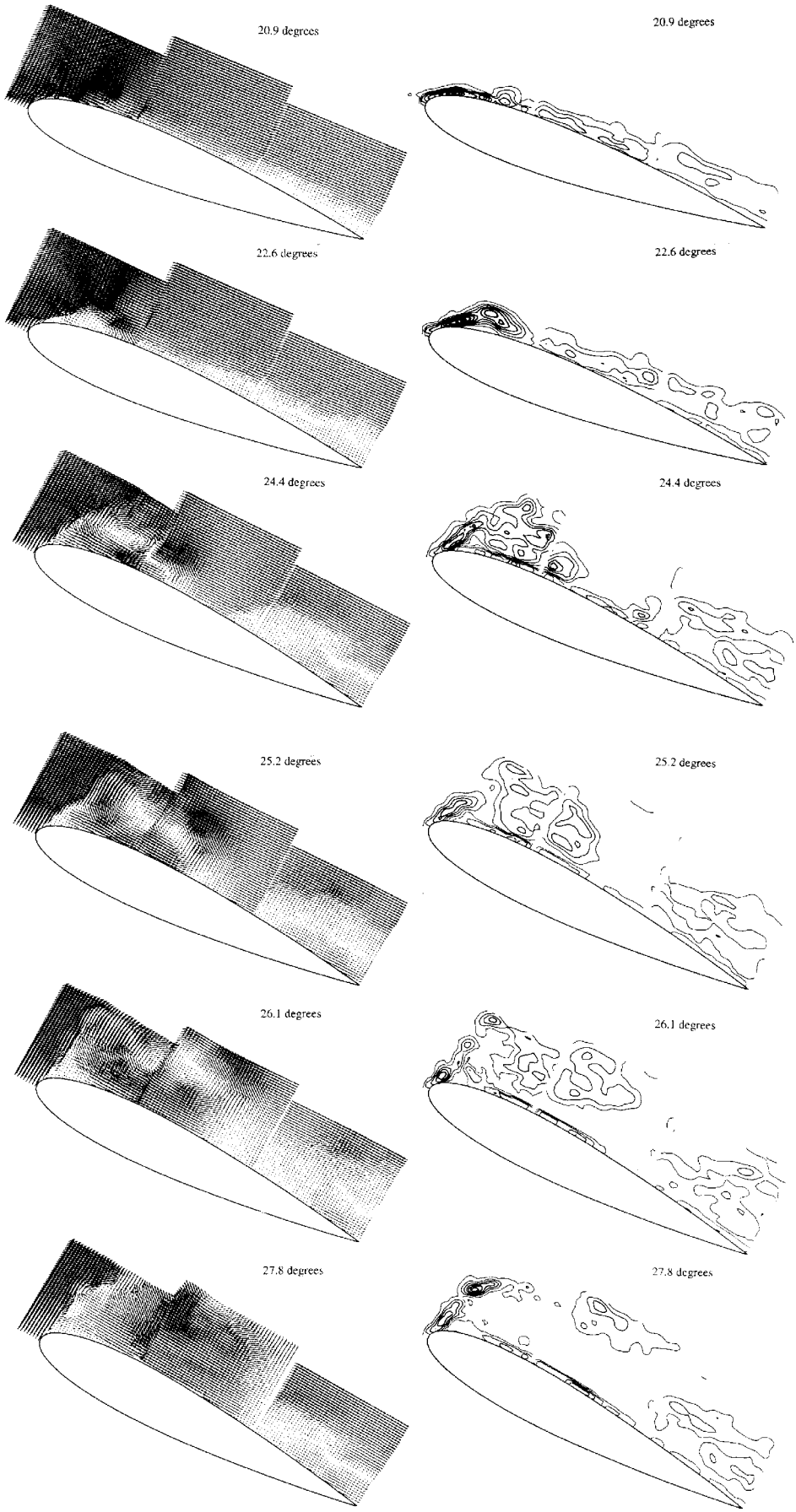

Fig. 3 Typical instantaneous velocity vectors and spanwise vorticity (ω_z) contours on the suction side of the airfoil; $Re = 1.5 \times 10^5$ and $\alpha^+ = 0.072$. Vorticity contours: minimum magnitude level = 7 units and contour interval = 14 units. Full lines represent clockwise (negative) vorticity, and dotted lines represent counterclockwise (positive) vorticity.

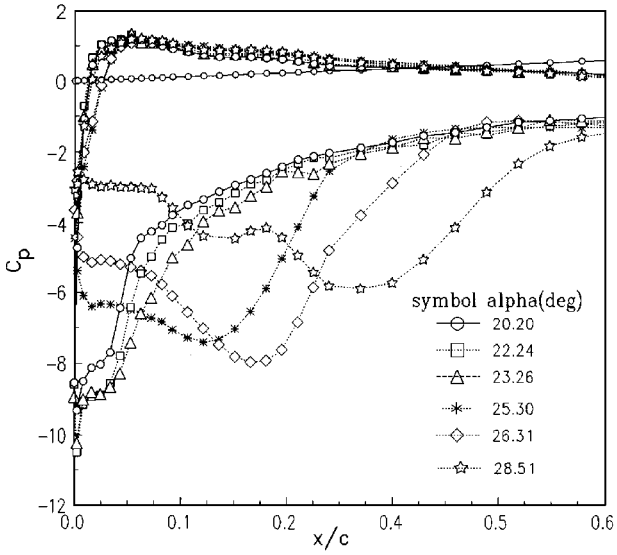

a) Surface pressure distributions

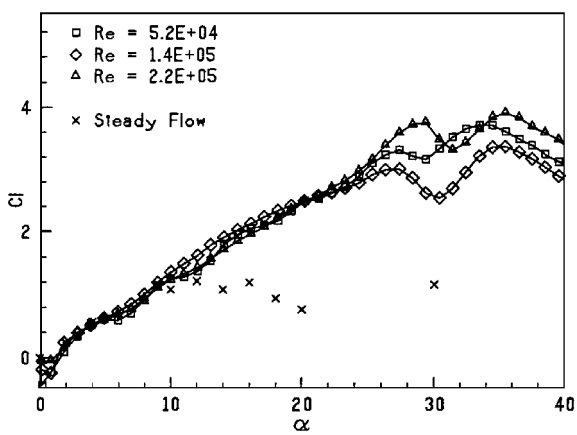

b) Lift

Fig. 4 Phase-locked surface pressure and lift data for the pitching airfoil at $Re = 1.5 \times 10^5$ and $\alpha^+ = 0.072$ (Ref. 6).

as can be seen typically from Fig. 3 for $\alpha = 22.6$ deg. The reverse flow from the trailing edge does not, however, seem to be the cause of the LEV formation in the front region of the airfoil, because it is physically separated from the LEV, as seen clearly from the vorticity contours at this incidence. The shear layer in the front region starts to bulge out because of the large adverse pressure gradient, which infuses positive (counterclockwise) vorticity at the surface. This causes the vorticity maximum to move away from the wall, causing the vorticity contours to form locally closed curves. A region of flow reversal seems to develop between the airfoil surface and the contours of negative vorticity convected from the leading edge, causing the shear layer of negative vorticity to lift up. The clockwise vorticity associated with this reverse flow is still too small to be visible in the vorticity contours shown for this incidence. Simultaneously, a plateau begins to appear in the pressure distributions near the leading edge. This can be seen typically form the pressure distribution for $\alpha = 22.24$ deg in Fig. 4a. However, the vorticity still remains concentrated close to the wall. The lift therefore continues to increase with incidence, as seen from Fig. 4b. As the incidence increases further beyond 22 deg, the reverse flow carrying the counterclockwise vorticity grows between the shear layer and the airfoil surface causing the shear layer to roll up. Also, during this period the shear layer appears to break down due to instability, forming several smaller vortices. A conglomeration of such shear layer vortices can typically be seen at $\alpha = 24.4$ deg in Fig. 3. The contours of counterclockwise vorticity now become visible underneath the primary vortex and are shown as dotted lines. These correspond to the so-called secondary vortex observed in the calculations of Choudhuri et al.[5] In fact, another vortex with clockwise vorticity, referred to by these authors as the tertiary vortex, can also be distinguished near the nose. This can be seen more clearly from the streamline patterns to be presented later.

The rolled-up shear layer and the conglomeration of the remnants of shear layer vortices can together be described as the dynamic-stall vortex (DSV). As the incidence increases, the DSV begins to grow very rapidly and move slightly downstream. The downstream convection of the DSV is, however, minimal and most of the vortex stays in the front region ($x/c < 0.3$). A second suction peak corresponding to the signature of the DSV begins to appear in the pressure distributions in the region during this incidence range. This suction peak increases in magnitude and moves downstream with the DSV, as can be seen from Fig. 4a. Earlier flow visualization studies and surface pressure measurements[9,10] have also indicated that the location of the DSV center coincides approximately with the location of the secondary peak in C_p distribution. The lift curve appears a little erratic during this period. Further increase in the incidence angle causes the DSV to enlarge rapidly, as can be seen from the results for $\alpha = 25.2$ deg. The shear layer gets pinched off at this incidence, as seen from the vorticity contours. However, the DSV is still located adjacent to the wall. It is ejected into the cross-stream direction at a slightly higher incidence of about 26 deg. The secondary vortical structure with positive vorticity grows beneath it, as seen from the vorticity contours for $\alpha = 25.2$ and 26.1 deg. Both the secondary suction peak and lift reach their maximum values slightly beyond $\alpha = 26$ deg. At the incidence of 27.8 deg, the DSV leaves our view and only a thin shear layer with a pair of shear layer vortices emanating from the leading edge can be seen. The dynamic stall has already occurred, and the suction peak and lift have dropped significantly from their maximum values. (Note that the second peak in the lift curve is most probably due to blockage effects that become significant after the occurrence of dynamic stall.)

Meanwhile, in the mid-to-aft regions, the separated layer originating from the trailing edge starts to form a second vortex, the so-called shear-layer vortex (SLV). The experiments indicated that, beyond an incidence of about 23 deg, the spacing between the two vortical regions increased and the two vortices became more distinct from each other. This can be clearly seen from both the velocity and vorticity results for $\alpha = 24.4$, 25.2, and 26.1 deg. These flow structures observed in the present experiments are qualitatively similar to the results of earlier flow visualization studies,[9,11] as well as numerical analyses,[12] at low Reynolds number (on the order of 10^4).

Reynolds Number Effects on the Flow Structure

Figures 5a and 5b show how the DSV is convected downstream after it is formed. The results are shown for the two Reynolds numbers

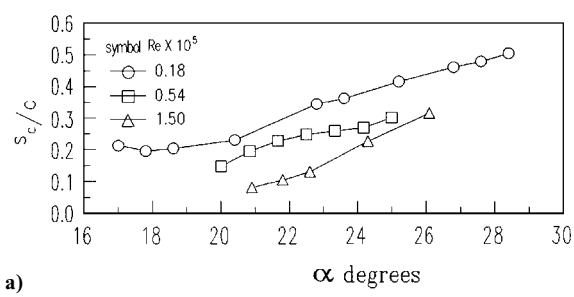

a)

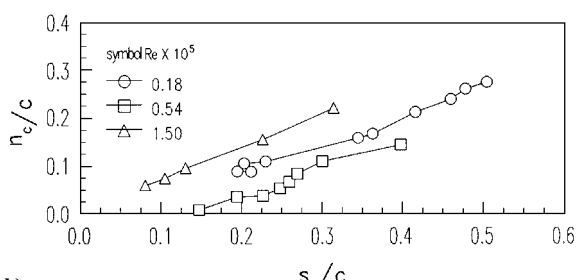

b)

Fig. 5 Effect of Reynolds number on the convection of the DSV.

studied in the present experiments and compared with the results obtained at the low Reynolds number of 1.8×10^4 in Ref. 2. Figure 5a shows the streamwise coordinate s_c of the center of the DSV as a function of the angle of incidence, whereas Fig. 5b shows the trajectory of the vortex center. The center of the DSV was determined by assuming it to coincide with the centroid of the vorticity distribution associated with the DSV. For this purpose, the domain of the DSV was subjectively inferred from observing the streamline pattern of the flow. Because of this reason, the results shown in Fig. 5 (especially the n/c values) should be used with some caution. However, it is quite clear from Fig. 5a that, within an uncertainty of about 1 deg in incidence (approximately one frame interval of the photographs), the LEV formation (in the sense of an identifiable vortex center) occurs at an incidence of 20–21 deg at both the higher Reynolds numbers. Likewise, the plots in both cases extend up to a maximum angle of incidence of about 26 deg. Beyond this incidence, the DSV is rapidly ejected in a direction almost normal to the airfoil surface into the freestream, which results in the vortex being either partially or fully outside the field of view. The location of the center of the vortex cannot therefore be ascertained. It was seen from Figs. 3 and 4 that this situation corresponds to dynamic stall. Hence, we can infer from Fig. 5a that the inception of the LEV and the onset of dynamic stall occur at nearly the same angles at both these higher Reynolds numbers. In contrast with this, the vortex inception occurs at an incidence of about 17 deg at $Re = 1.8 \times 10^4$. The vortex center in this case could be tracked all of the way up to the maximum angle of about 25 deg up to which the airfoil was pitched in that experiment. This tracking became possible because the DSV did not actually break away from the airfoil but remained instead within the field of view over the entire range of pitching, even though the shear layer was pinched off at about 24 deg. In fact, because of this and also because no lift measurements were made, it is not possible to confirm whether dynamic stall actually occurred or not in the experiment.

Unlike the incidence angle of LEV inception, the actual location of the vortex trajectory exhibited nonmonotonic behavior with respect to Reynolds number. This can be seen from Fig. 5b. Obviously, the data for the two Reynolds numbers studied in the present experiments do not collapse together, indicating that in this respect the flow exhibits Reynolds number dependence. However, the data do indicate that at all of the Reynolds numbers, the vortex center is convected with about the same constant velocity. The convection velocity calculated from the average trajectory slope is about $0.6\,U_\infty$.

The effect of Reynolds number on the detailed flow structure can be further examined with reference to Figs. 6a–6c, which compare the vorticity contours in the flow at the three Reynolds numbers. In each case, the specific angle of incidence selected for comparison corresponds to the instant after the shear layer detachment is complete. In the present experiments at the higher Reynolds numbers, this angle also corresponds to the instant just prior to the occurrence of dynamic stall. It is interesting to note that certain features such as the primary, secondary, and tertiary vortical structures are present at all of the Reynolds numbers. Now, to study the differences, let us first compare the results at the highest and lowest Reynolds numbers. The most striking difference between these two cases is in the extent of the wing surface over which the DSV has spread. At the lowest Reynolds number, the rolled-up shear layer contains a number of vortical structures that are remnants of vortices generated by the shear layer instability. The vorticity contours indicate that these remnants still carry a substantial amount of vorticity. Furthermore, even though the shear layer has just been pinched off, the DSV consisting of the conglomeration of the vortices is still within the view of the camera. The release of the DSV from the surface can be considered to be gradual and is in a direction approximately along the airfoil surface. In other words, the DSV has not really been torn away and ejected from the surface. In fact, such an ejection was not observed even at the incidence of 28.5 deg, which was the largest incidence measured in that experiment. In contrast to this, the release of the DSV at the highest Reynolds number is more in the nature of an abrupt ejection in a direction almost normal to the airfoil surface. The DSV in this case is also more compact and its severance from the shear layer is sharper. One can still observe several remnant vortical

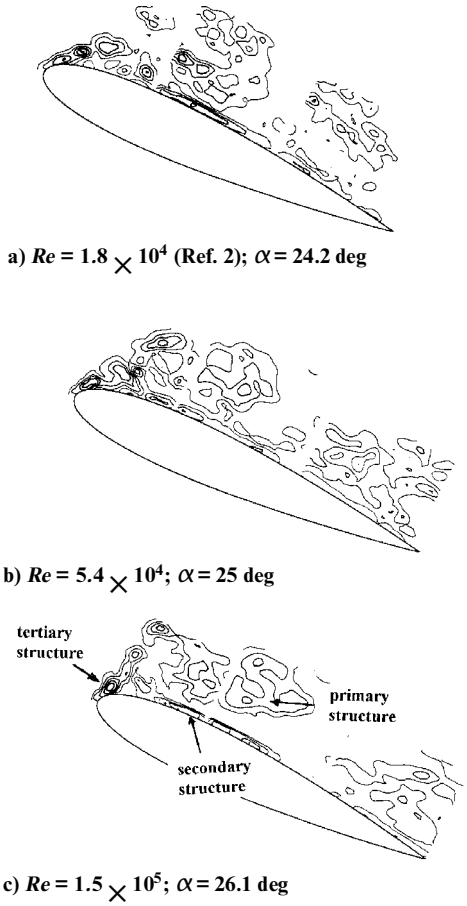

a) $Re = 1.8 \times 10^4$ (Ref. 2); $\alpha = 24.2$ deg

b) $Re = 5.4 \times 10^4$; $\alpha = 25$ deg

c) $Re = 1.5 \times 10^5$; $\alpha = 26.1$ deg

Fig. 6 Effect of Reynolds number on the vortical structure of the DSV; $\alpha^+ = 0.072$. In each case, the incidence corresponds to the instant just after shear layer detachment. Contour values same as in Fig. 3.

structures inside the DSV, but these are fewer in number, weaker, and less coherent than at the lowest Reynolds number. Apparently, at the highest Reynolds number, the breakdown of the shear layer due to instability occurs more slowly relative to the roll-up and ejection process. The latter is completed very rapidly even though it starts at a larger incidence than at the low Reynolds number. Since the nondimensional pitching rate was the same in all of these experiments, this indicates that the shear layer breakdown and roll-up/ejection are two different processes, each characterized by a different time scale. The rapidity with which the shear layer ejection occurs compared with the rate of formation of the instability vortices suggests that at high Reynolds numbers the process of dynamic stall is likely to be less sensitive to any attempt to alter the stability characteristics of the shear layer. Another significant feature that can be seen from Fig. 6 is that, as the Reynolds number increases, the DSV is more clearly separated from the SLV occupying the aft region of the airfoil.

The flow structure at the intermediate Reynolds number is somewhat similar to that at the highest Reynolds number in terms of the preceding details. Thus, there are only a small number of remnant vortical structures within the DSV and the shear layer is ejected nearly abruptly at a fairly large angle to the airfoil surface in both the cases. This similarity results in nearly identical lift generation characteristics at these two Reynolds numbers, as seen from Fig. 4b. The differences in some of the kinematic features such as cross-stream locations and trajectories at the two Reynolds numbers (observed in Fig. 5b) thus do not seem to significantly affect the gross flow dynamics. Unfortunately, lift data could not be obtained in the experiments of Ref. 2, and so a comparison cannot be made between the extreme Reynolds numbers.

The similarity in the flow structure observed at the two higher Reynolds numbers studied in the present experiments is believed to be due to the triggering of early transition over the airfoil by the high freestream turbulence (and consequent elimination of the laminar

separation bubble) at these Reynolds numbers. The Reynolds number of 1.8×10^4 studied in Ref. 2 was too small for such an early triggering of transition to occur, even with the high freestream turbulence. A very detailed discussion on the process of transition in these experiments has been presented in Ref. 6. The present PIV results from the experiments at Reynolds numbers of 5.4×10^4 and 1.5×10^5, in fact, provide further confirmation of the early triggering of transition.

Other Kinematic Features of the Flow

From the basic PIV data collected, it is possible to recover, in addition to the velocity and vorticity information presented earlier, other useful kinematic information such as the cross-stream distributions of strain rates, streamlines, and topology of the flow. Some typical results are presented next for the higher Reynolds number experiment. More extensive results for all of the Reynolds numbers, including detailed plots of the velocity and vorticity distributions across the flow, are available from Oshima.[8]

Strain Rate and Velocity Gradients

Figure 7a shows the contours of shear strain rate $\epsilon_{s,n}$, whereas Figs. 7b and 7c show contours of the individual velocity gradients $S_{s,n}$ and $S_{n,s}$, for an incidence of 25.2 deg (just prior to the occurrence of dynamic stall). Note that the sum of these velocity gradients represents the shear strain rate and their difference represents the vorticity, which is shown in Fig. 3. In all of the cases, the outermost contours have the same magnitude (of about 7 units) and the contour intervals are the same (about 14 units). It is seen that in the front region $S_{n,s}$ (showing 1 to 2 contour lines and a maximum value of about 21 units) is quite significant (about 60%) compared with $S_{s,n}$ (showing up to 3 contours and a maximum value of about 35 units). This

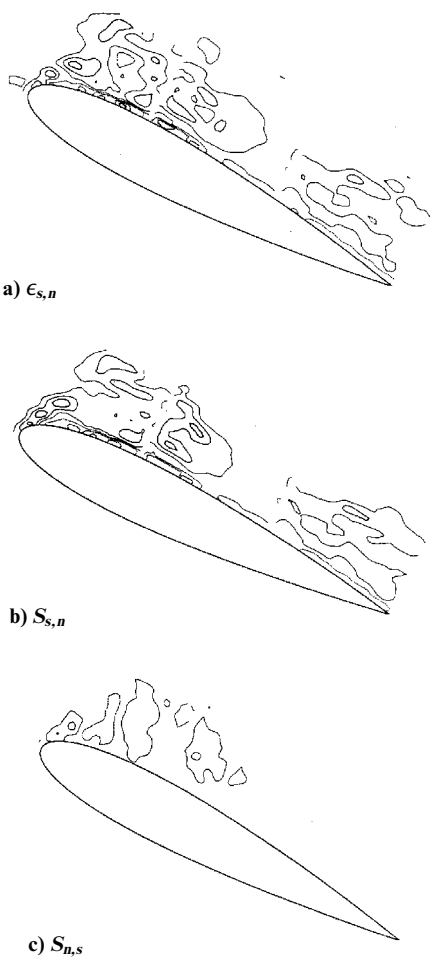

Fig. 7 Contours of the instantaneous shear strain rate and velocity gradients at an incidence of 25.2 deg (just after shear layer detachment): $Re = 1.5 \times 10^5$ and $\alpha^+ = 0.072$. Contour values same as in Fig. 3.

results in the vorticity and shear strain rates differing significantly from each other, as can be seen from a comparison of the vorticity contours in Fig. 3 with the shear strain contours in Fig. 7a. The shear strain rate contours are stretched out longer along the airfoil. On the other hand, in the rear part of the airfoil (occupied by the SLV), $S_{n,s}$ is less than 7 units in magnitudes (because its contours are not seen in Fig. 7c), whereas $S_{s,n}$ has a maximum magnitude of about 21 units. Hence, the vorticity, shear strain rate, and $S_{s,n}$ contours are all nearly identical to one another in this region. Note, however, that in all regions of the flow the magnitudes of $S_{n,s}$ are still significant enough to invalidate boundary-layer approximations at this incidence.

Streamline Pattern and Topology of the Flowfield

Figures 8a–8d show some selected streamline patterns from the experiment at $Re = 1.5 \times 10^5$ of the present study. These streamline patterns are as they appear to an observer moving with the airfoil. Because of the integration and smoothing involved in the calculation of the streamlines from the velocity data, only the strongest structures are seen. The details of the remnants of vorticity generated by the shear layer instability are therefore not visible in these patterns. Following the approach of Perry and Chong,[13] we can study from these figures the evolution of the topological features in the flow around the pitching airfoil in terms of the two types of critical points, namely, centers and saddles. It is seen that at the incidence of 20.9 deg the streamlines next to the surface in the front region start to thicken. This stage corresponds to the formation of the primary recirculation center C1 associated with the LEV near the leading edge within the thin layer next to the surface. Even though the PIV could not capture the details of the region because of its limited spatial resolution, the recirculation region can be identified by the bulging of the streamlines in the front region of the airfoil. Also, a distinctive half-saddle point (S1 in Fig. 8a) can be observed between the primary recirculation and the flow reversal from the trailing edge. The reverse flow near the trailing edge that started much earlier has already moved significantly upstream by this time.

The pair of critical points (a center C1 and a saddle S1) associated with the formation of the clockwise primary recirculation (or the LEV) can be more clearly observed at the incidence of 21.8 deg. During the incidence interval of 20.9–21.8 deg, the saddle point S1 moves downstream to the midregion, and a secondary recirculation region with counterclockwise rotation can be observed upstream of the LEV. The secondary recirculation has a center C2 (which is very close to the surface and hence cannot be seen very well from the PIV data) and a corresponding half-saddle point S2 upstream of the center. At the incidence of 22.6 deg, a third pair of critical points (C3 and S3) appears upstream of the other two recirculation regions to form a tertiary recirculating region associated with clockwise rotation. The saddle S3 associated with the third recirculating region is a full saddle located above the secondary recirculation. This recirculation region has been referred to as the tertiary vortex. Streamlines emanating from the leading edge encompass the three recirculating regions. Up to this incidence, streamline patterns in the aft region are relatively complex and it is hard to describe them using the critical point theory.

As the incidence increases, the primary recirculation region rapidly increases in size to form the DSV, which eventually begins to detach from the surface. Simultaneously, the coherent vortical structure of the SLV begins to form. These features can be seen from Fig. 8d, corresponding to an incidence of 25.2 deg. The three vortical structures near the leading edge associated with the centers C1, C2, and C3 are labeled in Figs. 8d and 6c for easy identification. The half-saddle point S1 associated with the primary recirculation (DSV) has just detached from the surface to form a full-saddle point. In the aft region, the vortical structures seem to have settled into two recirculating regions, exhibiting a pair of structures (C4, S4) and (C5, S5), even though the saddle point S4 associated with the SLV must be in the wake and is not seen in Fig. 8d.

Within the limitations of the spatial resolution of the PIV, the evolution of the dominant topological features of the flow, namely, the primary, secondary, and tertiary vortices, observed in the present experiments is in very good agreement with that computed numerically in Choudhuri et al.[5] for a pitching NACA 0012 airfoil at $Re = 10^4$ and $\alpha^+ = 0.2$. The similarity in the results in spite of the difference

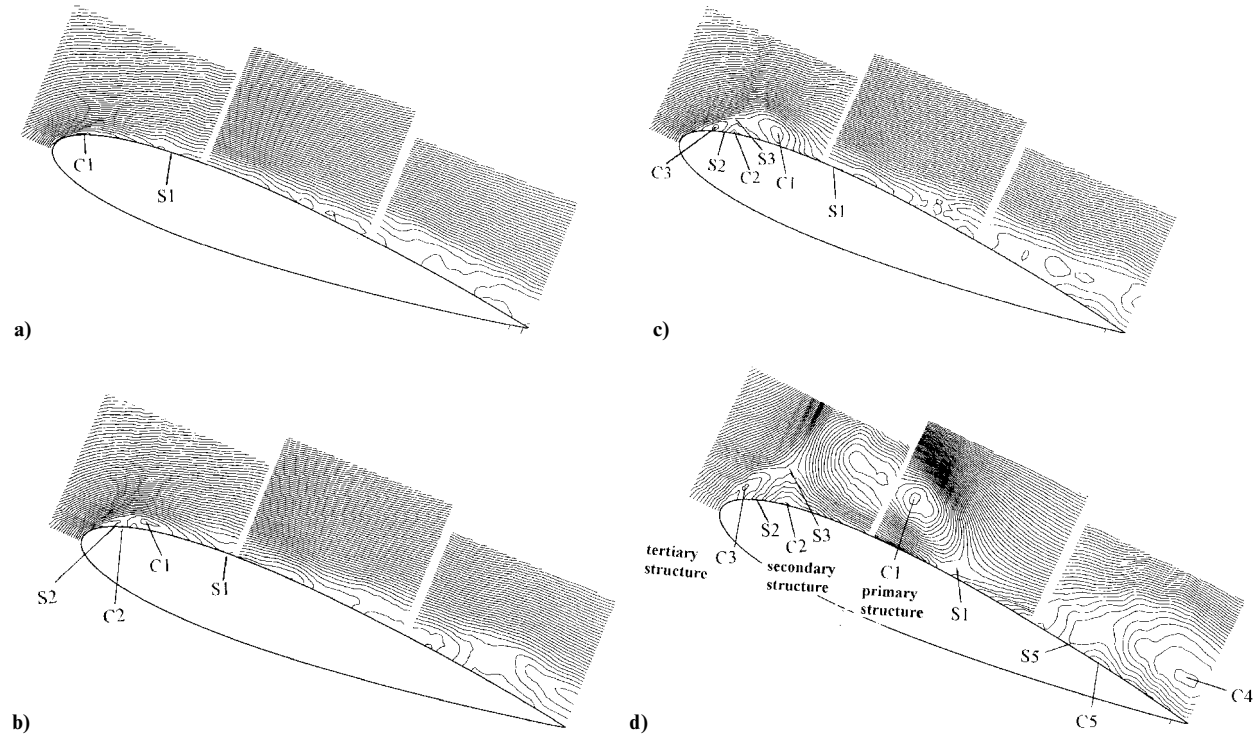

Fig. 8 Typical instantaneous streamline patterns in the flow at $Re = 1.5 \times 10^5$ and $\alpha^+ = 0.072$, showing the evolution of the pairs of centers C and saddle points S; a) $\alpha = 20.9$ deg, b) $\alpha = 21.8$ deg, c) $\alpha = 22.6$ deg, and d) $\alpha = 25.2$ deg.

in airfoil geometries, Reynolds numbers, nature of flow (laminar vs turbulent), and pitch rates suggests that the dominant topological features are possibly a generic property of two-dimensional unsteady separating flows.

Conclusions

1) The increase in lift of a pitching airfoil is due to the influx of vorticity from the surface by the presence of strong favorable pressure gradient near the leading edge. Lift continues to increase so long as vorticity is generated and remains close to the airfoil surface. Infusion of counterclockwise vorticity from the airfoil surface due to local adverse pressure gradient forces the shear layer to lift up and thus creates the LEV. Also, the continued influx of counterclockwise vorticity from the surface produces a secondary counterclockwise vortical structure underneath the LEV, which causes the shear layer to roll up. The rolled-up shear layer, along with the remnants of several vortices generated by the shear layer instability, forms the DSV. The DSV grows in size and is eventually ejected abruptly at a large angle with respect to the airfoil surface leading to the dynamic stall.

2) Early transition to turbulence at high Reynolds numbers causes the LEV to form at larger incidences, but more abruptly than at low Reynolds numbers. Also, the DSV at high Reynolds numbers is more compact and better defined and contains fewer remnant vortices formed from the instability of the shear layer before it is ejected from the surface at a steep angle. The DSV is clearly separated from another dominant vortical structure, the so-called SLV, which occupies the mid-to-aft region of the airfoil.

3) The dominant topological features observed in the leading-edge region of the flow are similar to those predicted in Ref. 5. They appear to be generic characteristics of unsteady separation.

The PIV data, along with the surface pressure data, have been archived and are available to any interested reader.

Acknowledgments

This work was supported by the U.S. Air Force Office of Scientific Research through Grants AFOSR-90-0131 and F49620-92-J-0146. This support is gratefully acknowledged.

References

[1]Shih, C., Lourenco, L., Van Dommelen, L., and Krothapalli, A., "Unsteady Flow Past an Airfoil Pitching at a Constant Rate," *AIAA Journal*, Vol. 30, No. 5, 1992, pp. 1153–1161.

[2]Oshima, H., and Ramaprian, B. R., "Measurement of the Velocity and Vorticity Fields Around a Pitching Airfoil," AIAA Paper 92-2626, June 1992.

[3]Ghia, K. N., Yang, J., Oswald, G. A., and Ghia, U., "Study of the Role of Unsteady Separation in the Formation of Dynamic Stall Vortex," AIAA Paper 92-0196, Jan. 1992.

[4]Visbal, M. R., and Shang, J., "Investigation of the Flow Structure Around a Rapidly Pitching Airfoil," *AIAA Journal*, Vol. 27, No. 8, 1989, pp. 1044–1051.

[5]Choudhuri, P. G., Knight, D. D., and Visbal, M. R., "Two-Dimensional Unsteady Leading-Edge Separation on a Pitching Airfoil," *AIAA Journal*, Vol. 32, No. 4, 1994, pp. 673–681.

[6]Conger, R. C., and Ramaprian, B. R., "Pressure Measurements on a Pitching Airfoil in a Water Channel," *AIAA Journal*, Vol. 32, No. 1, 1994, pp. 108–115.

[7]Conger, R. C., and Ramaprian, B. R., "The WSU-MME 1×0.7 m Water Channel," Dept. of Mechanical and Materials Engineering, Washington State Univ., Rept. MME-TF-92-1, Pullman, WA, Dec. 1992.

[8]Oshima, H., "PIV Studies of the Unsteady Vortex Dynamics of a Two-Dimensional Pitching Airfoil," Ph.D. Thesis, Dept. of Mechanical and Materials Engineering, Washington State Univ., Pullman, WA, Dec. 1994.

[9]Walker, J. M., Helin, H. E., and Strickland, J. H., "An Experiential Investigation of an Airfoil Undergoing Large Amplitude Pitching Motions," *AIAA Journal*, Vol. 23, No. 8, 1985, pp. 1141–1143.

[10]Walker, J. M., Helin, H. E., and Chou, D. C., "Unsteady Surface Pressure Measurements on a Pitching Airfoil," AIAA Paper 85-0532, March 1985.

[11]Lovato, J. A., "Active Control of the Separation Region on a Two-Dimensional Airfoil," Ph.D. Thesis, Dept. of Mechanical and Materials Engineering, Washington State Univ., Pullman, WA, June 1992.

[12]Visbal, M., "On Some Physical Aspects of Aerofoil Dynamic Stall," *Proceedings of the International Symposium on Non-Steady Fluid Dynamics*, ASME FED, edited by J. A. Miller and D. P. Telionis, Vol. 92, 1990, pp. 127–148.

[13]Perry, A. E., and Chong, M. S., "A Description of Eddying Motions and Flow Patterns Using Critical-Point Concepts," *Annual Review of Fluid Mechanics*, Vol. 19, 1987, pp. 125–155.